Scripta Materialia 122 (2016) 5–9

Contents lists available at ScienceDirect

Scripta Materialia

journal homepage: www.elsevier.com/locate/scriptamat

Regular Article

Coupling electron beam melting and spark plasma sintering: A new processing route for achieving titanium architectured microstructures

Guilhem Martin [a,b,*], Damien Fabrègue [c], Florian Mercier [c], Juan-Antonio Chafino-Aixa [c], Rémy Dendievel [a,b], Jean-Jacques Blandin [a,b]

[a] Université Grenoble Alpes, SIMAP, F-38000 Grenoble, France
[b] CNRS, SIMAP, F-38000 Grenoble, France
[c] MATEIS, INSA-Lyon, CNRS UMR5510, F-69621, France

ARTICLE INFO

Article history:
Received 18 March 2016
Received in revised form 28 April 2016
Accepted 1 May 2016
Available online 24 May 2016

Keywords:
Additive manufacturing
Spark plasma sintering
Titanium alloys
Microstructure
Metal-metal composites

ABSTRACT

A new route for elaborating architectured materials with a spatially controlled 3D microstructure is proposed. A combination of Electron Beam Melting (EBM) and Spark Plasma Sintering (SPS) is used to generate a microstructural composite made of Ti-alloys. A lattice structure made of Ti6Al4V is first fabricated by EBM. The lattice structure is then filled with another Ti-alloy powder before SPS. A bulk specimen is thus obtained with two different microstructures: one inherited from the EBM process in the lattice and the other one resulting from sintering in the matrix.

Architectured materials are, according to the definition given by Ashby in [1], combinations of two or more materials, or of materials and space, assembled in such a way as to achieve properties (e.g. toughness, work hardening capacity, ductility, electrical or thermal conductivity) not offered by a monolithic material. Exploring the potential of architectured materials requires to emphasize the choice of components, their relative volume fraction, their 3D arrangement as well as the way they are connected to each other [2]. Most of the architectured materials investigated in the literature have been cellular structures, i.e. combining material and space. Architectured microstructures would suggest that one can control in 3D the spatial arrangement of various microstructures. Being able to produce architectured microstructure could be of interest to achieve novel properties that would be impossible to obtain using only one microstructure.

In the present contribution we explore an innovative route to achieve Ti-Ti architectured microstructures exhibiting a well-controlled 3D arrangement of the different constituents by combining two existing processes: Electron Beam Melting (EBM) and Spark Plasma Sintering (SPS). Additive Manufacturing (AM) technologies have revolutionized the production of Ti-alloys parts (e.g. [3–5]) making possible the production of parts with a high degree of freedom in design. In addition, SPS enables to consolidate easily and quickly metallic materials, limiting microstructural evolution such as grain growth, see e.g. for Ti-alloys [14–16] or pure Fe [17].

EBM is used to perfectly control the 3D spatial distribution of the first constituent of the architectured microstructure, typically following the frame of a lattice structure [3–13]. SPS is then used to fill in the remaining space. We demonstrate through two different examples that the combination of EBM and SPS turns out to be a very promising way of elaborating Ti-Ti architectured microstructures with a well-controlled 3D arrangement. Through this new processing route spatially controlled mixtures of hard and soft microstructures can be achieved.

The prealloyed Ti6Al4V powder was fabricated by plasma atomization and provided by ARCAM. Two different batches of Ti6Al4V powders were used. One powder batch will be denoted *as-received* and meets the standard in terms of chemical composition for the Ti6Al4V alloy (Table 1). The second batch will be denoted *re-used* and resulted from as received powders that were re-used 20 times in the EBM process. The *as-received* Ti6Al4V powder batch shows a near perfectly spherical morphology (good flowability) with a limited number of satellites as well as a particle size distribution between 45 and 100 μm. The *re-used* Ti6Al4V powder batch (O-enriched) did not show significant differences when compared to the *as-received* batch in terms of morphology and size distribution. The main difference between both Ti6Al4V powder batches was the oxygen content as shown in Table 1. Oxygen contamination of the Ti6Al4V powders when using powders that have been many times re-used is a well-known process in parts made by

* Corresponding author.
E-mail address: guilhem.martin@simap.grenoble-inp.fr (G. Martin).

http://dx.doi.org/10.1016/j.scriptamat.2016.05.001
1359-6462/

Table 1
Chemical composition in %wt of the powder batches used in the present investigation.

	%Al	%V	%Fe	%N	%C	%O
Ti6Al4V *as-received*	6.18	4.15	0.21	0.05	0.01	0.19
Ti6Al4V *re-used*	5.84	4.11	0.21	0.05	0.01	0.44
Ti-Grade 2	–	–	<0.3	<0.03	<0.10	<0.25

EBM [18,19]. Note that in the same time the aluminum content has slightly decreased and that was attributed to the evaporation of Al during the process [20].

The commercially pure titanium powders (CP-Ti Grade 2) were fabricated using the Plasma Rotated Electron Process (PREP) by STARMET. The CP-Ti Grade 2 which chemical composition is shown in Table 1, exhibits a spherical morphology but with a coarser size distribution (150–300 μm) compared to the one of the Ti6Al4V alloy (45–100 μm).

Lattice structures were first fabricated by electron beam melting starting from Ti6Al4V *re-used* powder (O-enriched) using an ARCAM A1 EBM machine (Fig. 1a–c). The structure of interest is the octet truss lattice structure made of 1 mm diameter struts [12,21], see Fig. 1c. The EBM process has been widely described in the literature, see e.g. [22,23]. The process occurs under vacuum, typically 2.10^{-3} mbar. The Ti6Al4V *re-used* powder, denoted *powder A* in Fig. 1a, is dispersed by raking on a 10 mm thick stainless steel start plate by layers of 50 μm. Then each powder layer is slightly sintered using a strongly defocused electron beam and subsequently selectively melted according to the input geometry. The lattice structures were fabricated using standard process parameters recommended by ARCAM.

A lattice structure was then introduced into a graphite die with 20 mm internal diameter and *powder B* was subsequently added to fill in the die, see Fig. 1c–e. The powder was finally consolidated by spark plasma sintering (SPS) at 900 °C for 10 min under vacuum (~10^{-2} mbar) and applying a pressure of 60 MPa, see Fig. 1f. If one wants to avoid to plastically deform the lattice structure during the SPS thermomechanical path, the latter has to be selected and sized adequately. The heating and cooling rate during sintering were set to 100 °C/min. The temperature was measured by pyrometry. It would be worth mentioning that a temperature difference of about 50 °C may exist between the actual temperature reached by the powder during spark plasma sintering and the temperature measured by pyrometry.

Microstructural characterizations were performed using optical microscopy as well as EBSD. Specimens were prepared by grinding and polishing using 1200-grit SiC paper and a solution consisting of 70% colloidal silica suspension (0.04 μm) and 30% H_2O_2. The microstructures were revealed using Kroll's reagent (2 ml HF + 4 ml HNO_3 in 100 ml of distilled H_2O). EBSD characterizations were performed using a step size of 0.2 μm. Based on the existence of the Burgers orientation relationship between the body-centered cubic β phase and the hexagonal α phase, a numerical reconstruction of the parent β grains, from the room temperature α phase EBSD data, was performed. A detailed description of the reconstruction procedure can be found in [24,25].

The mechanical properties of the microstructural composites were evaluated by microhardness measurements using a Wilson Tukon 1102 Vickers Tester. 12 × 12 mm Microhardness maps were performed using a 300*g* load on as polished 2D sections of the samples. The step size was set to 200 μm resulting in 3600 microhardness measurements covering the region of interest.

The struts constituting the lattice structure were almost fully dense (>99.5%) with only a few spherical pores (entrapped gas inherited from the atomization process [22]). The struts exhibit surface irregularities which have been attributed to unmelted powder particle stuck to the melt pool during the EBM process, see Fig. 2a–b. The microstructure of the α-phase was found to be similar whatever the strut orientation with respect to the build direction. The microstructure of the as-built octet truss lattice structure fabricated by EBM is lamellar, with fine Widmanstatten α laths oriented in various directions, see Fig. 2c. Although some α colonies – i.e. parallel α laths belonging to the same variant of the Burgers relationship – can be observed, most α platelets are individual, which is indicative of a relatively fast cooling rate during the β to α phase transformation. Their average width was measured to be about ~1.6 ± 0.2 μm. A continuous α_{GB} layer can be observed along

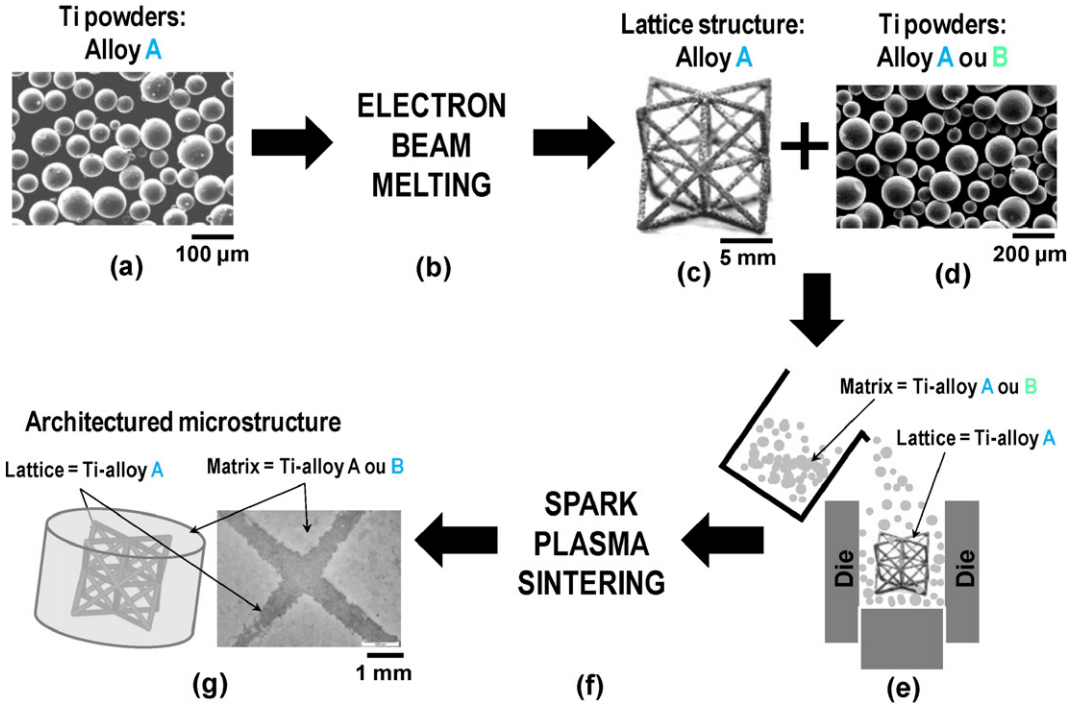

Fig. 1. Overview of the innovative route to produce Ti-Ti architectured microstructures. (a) Raw material for producing lattice structures (powder A). (b) EBM process. (c) Lattice structure produced by EBM. (d) Raw material for the matrix (powder B). (e) Introduction of the lattice structure into the die and filling with powder B. (f) SPS process. (g) Ti-Ti architectured microstructures.

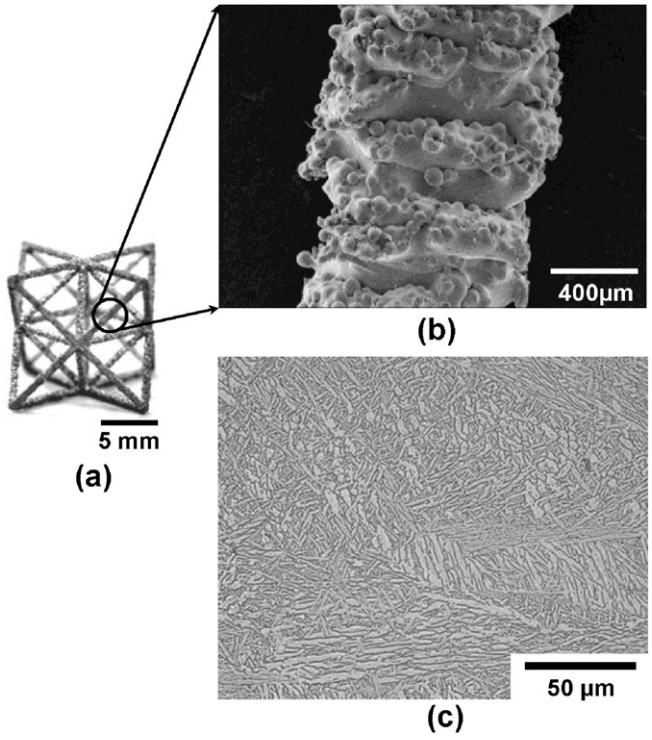

Fig. 2. (a) Unit cell of the octet truss lattice structure fabricated by EBM. (b) SEM micrograph showing powder particle stuck to a strut. (c) Typical microstructure observed in the *as*-built lattice structure.

some grain boundaries of the prior β grain boundaries. This observation is in agreement with the literature [26–28] though some authors have reported the presence of α′-martensite in thin struts fabricated by EBM [10]. In the present work, α′-martensite was not observed in the fabricated lattice structures.

As a proof of concept, two different Ti-Ti architectured microstructures were generated using the innovative fabrication route summarized in Fig. 1. Both samples were almost fully dense (>99%), only a few pores were still observed in 2D cross sections, see e.g. Fig. 3a. Surprisingly, there was not any preference for the pores to be located. In other words, pores were not preferentially located at the interface between the lattice and the matrix. This is clearly highlighted in Fig. 3e where an EBSD Index Quality (IQ) map showing the interface between the lattice and the matrix is displayed. In Fig. 3e, we can see that the matrix fits closely the surface irregularities (unmelted powder particles) of the struts.

The first Ti-Ti architectured microstructure was fabricated using a lattice structure made of Ti6Al4V *re-used* powders (%O = 0.44) filled with CP-Ti Grade 2 powders, see Fig. 3a. Within the lattice, the microstructure obtained after the SPS thermomechanical path (900 °C/10 min under 60 MPa) is very similar to that of the as-built material, in terms of morphology and size, see Fig. 3c. It means that the EBM microstructure is preserved after SPS. This was assessed by comparing the average thickness of the Widmanstatten α-laths before and after spark plasma sintering in the lattice. After SPS, Widmanstatten α-laths have an average thickness of ~1.8 ± 0.2 μm. In the EBM as-built microstructure, i.e. before SPS, the Widmanstatten α-laths exhibit a typical thickness 1.6 ± 0.2 μm). No significant microstructural evolution such as α laths coarsening was observed. The relatively short duration of the thermomechanical treatment (only 10 min at 900 °C) was not sufficient to achieve significant coarsening of the α-laths and the cooling rate of 100 °C/min was enough to achieve similar α-lath thickness (1.8 ± 0.2 μm). However, the matrix made of CP-Ti Grade 2, shows a significantly different microstructure compared to the one of the lattice. The matrix consisted of α coarse lamellae (width ~ 9 ± 1 μm) separated by very fine residual β, see Fig. 3b. Note that unlike the lattice, only one or two α colonies (same orientation) were observed within the

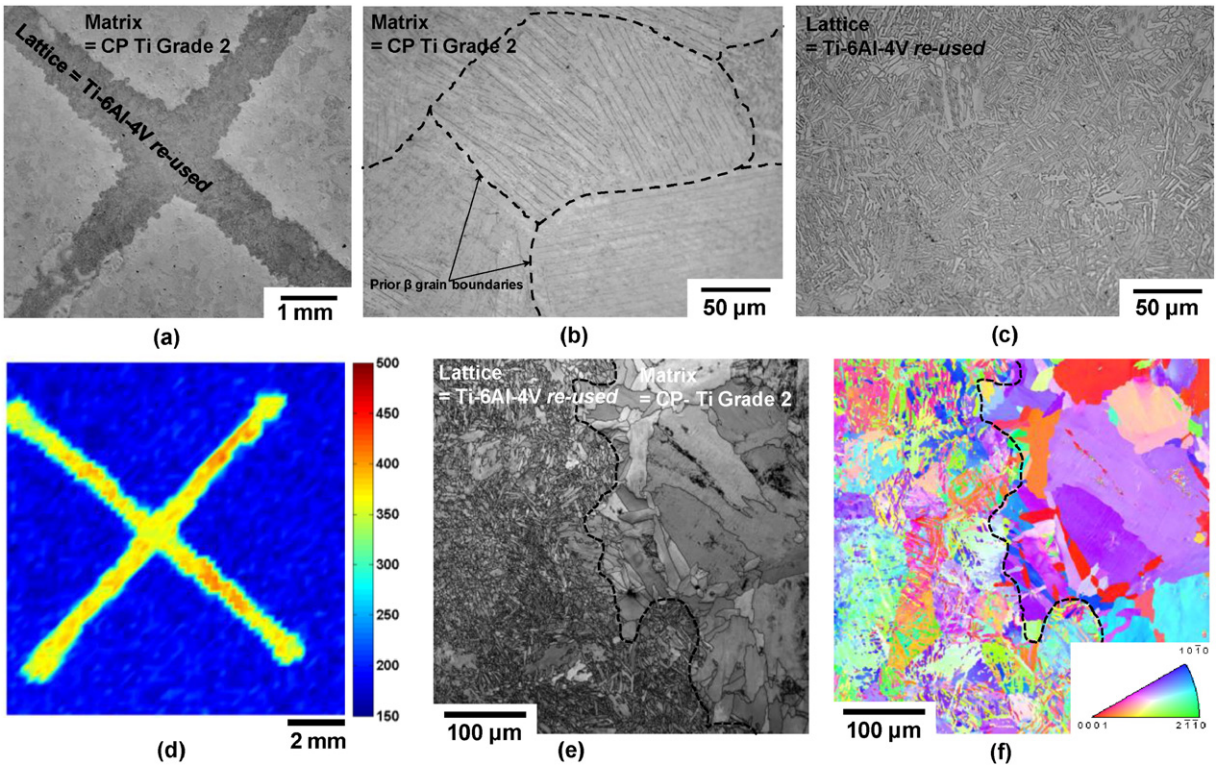

Fig. 3. Ti-Ti architectured microstructure consisting of a lattice made with re-used Ti6Al4V powder and a matrix made of CP-Ti Grade 2 powder. Multiscale optical micrographs: (a) macroscopic view (b) microstructure within the matrix and (c) within the lattice. (d) Microhardness map. EBSD characterization of the interface between the lattice and the matrix: (e) IQ map and (f) IPF Map of the room temperature α phase.

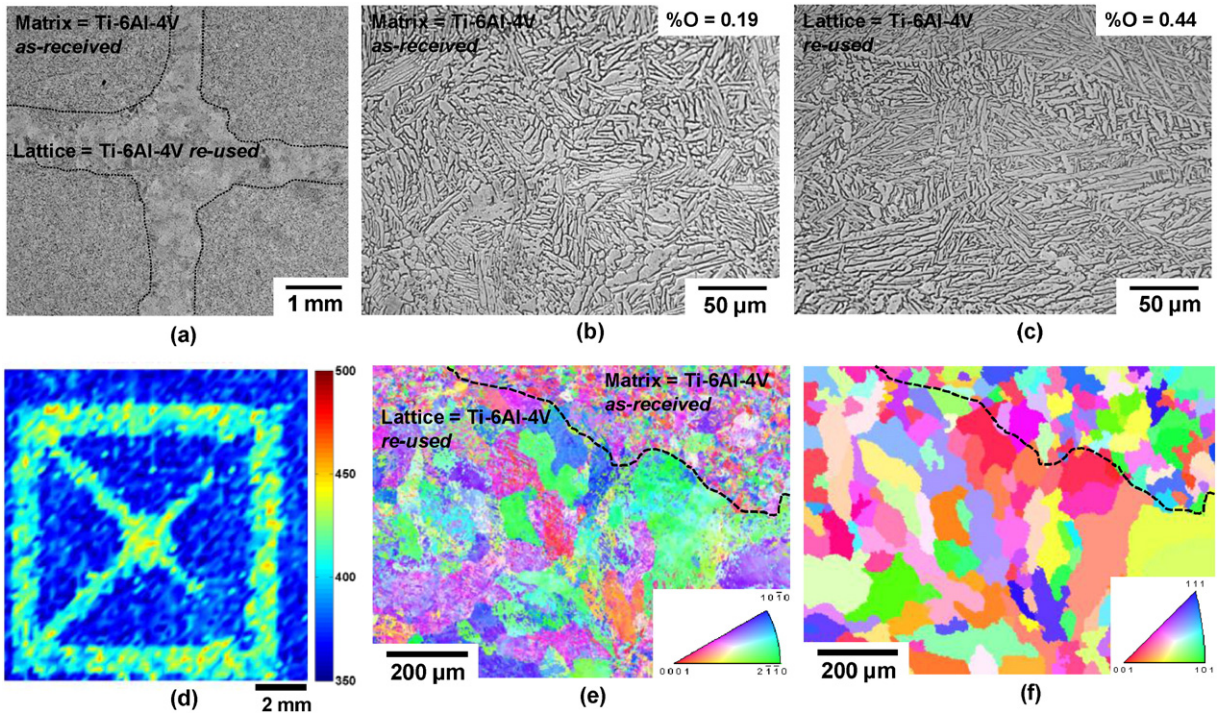

Fig. 4. Ti-Ti architectured microstructure consisting of a lattice made with re-used Ti6Al4V powder and a matrix made of as-received Ti6Al4V powder. Multiscale optical micrographs: (a) macroscopic view (b) microstructure within the matrix and (c) within the lattice. (d) Microhardness map. EBSD characterization of the interface between the lattice and the matrix: (e) IPF Map of the room temperature α phase and (f) IPF map of the reconstructed high temperature β grains.

high temperature β grains of the matrix, see the EBSD map shown in Fig. 3e–f. Prior β grains are decorated by α_{GB} and can be easily seen in Fig. 3b. The relatively coarse β grains suggest that the temperature achieved by the powder during the SPS operations was most likely higher than the β-transus of CP-Ti Grade 2 which is about 910 °C. The microhardness map that was performed on a 2D cross section is shown in Fig. 3d. The measurements are represented as a color map corresponding to different Vickers hardness values. The pattern of the lattice structure is well defined indicating that a Ti-Ti architectured microstructure with controlled heterogeneous mechanical properties was successfully fabricated. A pronounced mechanical contrast between the lattice (395 ± 15 HV) and the matrix (190 ± 15 HV) is found as highlighted in Fig. 3d. This result was expected based on the difference of alloying elements between the lattice fabricated using Ti6Al4V powders (%O = 0.44) and the matrix made of CP-Ti Grade 2, see Table 1.

The second Ti-Ti architectured microstructure was fabricated using a lattice structure made of Ti6Al4V *re-used* powders (%O = 0.44) filled with Ti6Al4V *as-received* powders (%O = 0.19), see Fig. 4a. This difference in %O should enable to achieve a difference of hardness between the lattice and the matrix. Indeed, solid solution hardening by interstitial oxygen is a well-known phenomenon in Ti-alloys [19,29]. Oh et al. [29] reported that an increase of 0.1%O in the Ti6Al4V alloy led to an increase of hardness of about 30 HV. Similar microstructures were observed within the lattice and the matrix, see Fig. 4b–c. The microstructure observed in the lattice and within the matrix were very similar to the one of the EBM as-built material, i.e. a two phase microstructure with fine Widmanstatten α-laths (width ~ 1.8 ± 0.2 μm) separated by fine regions of residual β (Fig. 4b–c). The matrix microstructure, resulting from the consolidation of the *as-received* Ti6Al4V powder, consisted of a similar microstructure, i.e. a fine α + β Widmanstatten microstructure with α-laths about 1.8 ± 0.2 μm in width. The main difference between the microstructure within the lattice and within the matrix could only be revealed by the numerical reconstruction of the β grains, see Fig. 4e–f. The lattice structure resulting from the solidification during the EBM process exhibits relatively coarse β grains (>50 μm). Within the matrix, the prior β grains have a much smaller size (~10 μm) because sintering was performed at 900 °C, i.e. below the β-transus of the Ti6Al4V alloy. The corresponding microhardness map is displayed in Fig. 4d. There was a difference of hardness between the lattice and the matrix: the average hardness value within the lattice was found to be about 405 ± 15 HV whereas within the matrix it was about 350 ± 15 HV. This hardness difference between the lattice and the matrix was expected based on the oxygen content which was significantly higher in the Ti6Al4V powder batch used for the lattice (%O = 0.44) compared to the one used for the matrix (%O = 0.19). This result is consistent with the results reported by Oh et al. [29].

An innovative route for the fabrication of architectured microstructures by coupling additive manufacturing and spark plasma sintering has been described. This process was demonstrated to be efficient for generating architectured microstructures made of Ti alloys.

Two different Ti-Ti architectured microstructures were successfully fabricated: one combining two different powder batches of the Ti6Al4V alloy differing from their oxygen content, and a second one combining the Ti6Al4V alloy with a CP-Ti Grade 2. For both composites, different microstructures and hardness were observed in the lattice and in the matrix. This new process definitely opens new avenues to achieve complex architectured microstructures when using the same material for the lattice and the powder, as well as to manufacture multi-materials when using different materials for the lattice and the powder. In addition it has to be highlighted that numerous additional options are available to generate a high variety of materials and microstructures. For instance, different microstructures between the lattice and the matrix can be generated by applying a pre-heat treatment on the lattice or by milling the powder before sintering. Exploring all these possibilities is the aim of an ongoing research.

Acknowledgements

This work was performed within the framework of the Center of Excellence of Multifunctional Architectured Materials "CEMAM" no. AN-10-LABX-44-01 funded by the "Investments for the Future Program".

References

[1] M. Ashby, Scr. Mater. 68 (2013) 4–7.
[2] N.A. Fleck, V.S. Deshpande, M.F. Ashby. Micro-architectured materials: past, present and future, Proceedings of the Royal Society A-Mathematical Physical and Engineering Sciences 466 (2010).
[3] P. Heinl, A. Rottmair, C. Koerner, R.F. Singer, Adv. Eng. Mater. 9 (2007) 360–364.
[4] P. Heinl, L. Mueller, C. Koerner, R.F. Singer, F.A. Mueller, Acta Biomater. 4 (2008) 1536–1544.
[5] L.E. Murr, S.M. Gaytan, F. Medina, E. Martinez, J.L. Martinez, D.H. Hernandez, B.I. Machado, D.A. Ramirez, R.B. Wicker, Materials Science and Engineering A-Structural Materials Properties Microstructure and Processing 527 (2010) 1861–1868.
[6] P. Heinl, C. Koerner, R.F. Singer, Adv. Eng. Mater. 10 (2008) 882–888.
[7] N.W. Hrabe, P. Heinl, B. Flinn, C. Koerner, R.K. Bordia. Compression-compression fatigue of selective electron beam melted cellular titanium (Ti-6Al-4V), Journal of Biomedical Materials Research Part B-Applied Biomaterials 99B (2011) 313-320.
[8] X.Y. Cheng, S.J. Li, L.E. Murr, Z.B. Zhang, Y.L. Hao, R. Yang, F. Medina, R.B. Wicker, J. Mech. Behav. Biomed. Mater. 16 (2012) 153–162.
[9] S.J. Li, L.E. Murr, X.Y. Cheng, Z.B. Zhang, Y.L. Hao, R. Yang, F. Medina, R.B. Wicker, Acta Mater. 60 (2012) 793–802.
[10] L.E. Murr, S.M. Gaytan, F. Medina, H. Lopez, E. Martinez, B.I. Machado, D.H. Hernandez, L. Martinez, M.I. Lopez, R.B. Wicker, J. Bracke, Philosophical Transactions of the Royal Society A-Mathematical Physical and Engineering Sciences 368 (2010) 1999–2032.
[11] E. Hernandez-Nava, C.J. Smith, F. Derguti, S. Tammas-Williams, F. Leonard, P.J. Withers, I. Todd, R. Goodall, Acta mater. 85 (2015) 387–395.
[12] M. Suard, G. Martin, P. Lhuissier, R. Dendievel, F. Vignat, J.J. Blandin, F. Villeneuve, Additive Manufacturing 8 (2015) 124–131.
[13] M. Suard, P. Lhuissier, R. Dendievel, J.J. Blandin, F. Vignat, F. Villeneuve. Towards stiffness prediction of cellular structures made by electron beam melting (EBM), powder Metall. 57 (2014) 190-195.
[14] S.K. Vajpai, K. Ameyama, M. Ota, T. Watanabe, R. Maeda, T. Sekiguchi, G. Dirras, D. Tingaud, 6th International Conference on Nanomaterials by Severe Plastic Deformation (NanoSPD), vol. 63, Metz, France, 2014.
[15] S.K. Vajpai, M. Ota, T. Watanabe, R. Maeda, T. Sekiguchi, T. Kusaka, K. Ameyama, Metallurgical and Materials Transactions A-Physical Metallurgy and Materials Science 46A (2015) 903–914.
[16] O. Ertorer, T.D. Topping, Y. Li, W. Moss, E.J. Lavernia, Metallurgical and Materials Transactions A-Physical Metallurgy and Materials Science 42A (2011) 964–973.
[17] D. Fabregue, J. Piallat, E. Maire, Y. Jorand, V. Massardier-Jourdan, G. Bonnefont, powder Metall. 55 (2012) 76–79.
[18] A. Strondl, O. Lyckfeldt, H. Brodin, U. Ackelid, JOM 67 (2015) 549–554.
[19] H.P. Tang, M. Qian, N. Liu, X.Z. Zhang, G.Y. Yang, J. Wang, JOM 67 (2015) 555–563.
[20] V. Juechter, T. Scharowsky, R.F. Singer, C. Koerner, Acta Mater. 76 (2014) 252–258.
[21] V.S. Deshpande, N.A. Fleck, M.F. Ashby, Journal of the Mechanics and Physics of Solids 49 (2001) 1747–1769.
[22] S. Tammas-Williams, H. Zhao, F. Leonard, F. Derguti, I. Todd, P.B. Prangnell, Mater. Charact. 102 (2015) 47–61.
[23] L.E. Murr, S.M. Gaytan, D.A. Ramirez, E. Martinez, J. Hernandez, K.N. Amato, P.W. Shindo, F.R. Medina, R.B. Wicker, Journal of Materials Science & Technology 28 (2012) 1–14.
[24] C. Cayron, B. Artaud, L. Briottet, Mater. Charact. 57 (2006) 386–401.
[25] C. Cayron, J. Appl. Crystallogr. 40 (2007) 1183–1188.
[26] S.S. Al-Bermani, M.L. Blackmore, W. Zhang, I. Todd, Metallurgical and Materials Transactions A-Physical Metallurgy and Materials Science 41A (2010) 3422–3434.
[27] C. de Formanoir, S. Michotte, O. Rigo, L. Germain, S. Godet, Materials Science and Engineering: A 652 (2016) 105–119.
[28] A.A. Antonysamy, J. Meyer, P.B. Prangnell, Mater. Charact. 84 (2013) 153–168.
[29] J.M. Oh, B.G. Lee, S.W. Cho, S.W. Lee, G.S. Choi, J.W. Lim. Oxygen Effects on the Mechanical Properties and Lattice Strain of Ti and Ti-6Al-4V, Met. Mater. Int. 17 (2011) 733–736.